

ExoplaNNet: A deep learning algorithm to detect and identify planetary signals in radial velocity data

L. A. Nieto^{1,2} & R. F. Díaz²

¹ Gerencia de Tecnología de la información y de las Comunicaciones (GTIC), Subgerencia Vinculación y Desarrollo de Nuevas Tecnologías de la Información, DCAP-CNEA. Centro Atómico Constituyentes, Av. Gral. Paz 1499, (1650) Buenos Aires, Argentina.

² International Center for Advanced Studies (ICAS) and ICIFI (CONICET), ECyT-UNSAM, Campus Miguelete, 25 de Mayo y Francia, (1650) Buenos Aires, Argentina.

Received TBC; accepted TBC

ABSTRACT

The detection of exoplanets with the radial velocity method consists in detecting variations of the stellar velocity caused by an unseen sub-stellar companion. Instrumental errors, irregular time sampling, and different noise sources originating in the intrinsic variability of the star can hinder the interpretation of the data, and even lead to spurious detections.

In recent times, work began to emerge in the field of extrasolar planets that use Machine Learning algorithms, some with results that exceed those obtained with the traditional techniques in the field. We seek to explore the scope of the neural networks in the radial velocity method, in particular for exoplanet detection in the presence of correlated noise of stellar origin.

In this work, a neural network is proposed to replace the computation of the significance of the signal detected with the radial velocity method and to classify it as of planetary origin or not. The algorithm is trained using synthetic data of systems with and without planetary companions. We injected realistic correlated noise in the simulations, based on previous studies of the behaviour of stellar activity. The performance of the network is compared to the traditional method based on null hypothesis significance testing.

The network achieves 28 % fewer false positives. The improvement is observed mainly in the detection of small-amplitude signals associated with low-mass planets. In addition, its execution time is five orders of magnitude faster than the traditional method.

The superior performance exhibited by the algorithm has only been tested on simulated radial velocity data so far. Although in principle it should be straightforward to adapt it for use in real time series, its performance has to be tested thoroughly. Future work should permit evaluating its potential for adoption as a valuable tool for exoplanet detection.

Key words. Methods: data analysis – Techniques: radial velocities – Planets and satellites: detection

1. Introduction

The study of extrasolar planets is a relatively new field of research. Although the first evidence of the existence of this type of bodies dates from 1917 (Landau 2017), it was not until the 1990s that the first confirmed detections took place. In 1992, by analysing the variations in the period of the pulses received from the radio millisecond pulsar PSR1257+12 Wolszczan & Frail (1992) concluded that at least two Earth-mass planets are in orbit around the pulsar. Three years later, Mayor & Queloz (1995) discovered the first exoplanet orbiting a solar-type star, 51 Peg b, by measuring the variations in the line-of-sight (radial) velocity of the host star induced by the unseen companion. In the years that followed this first detection, the radial velocity technique allowed unveiling a large number of planet candidates and information-rich systems, some with masses as small as a few times the mass of the Earth (e.g. Lovis et al. 2006; Mayor et al. 2009; Wright et al. 2016; Anglada-Escudé et al. 2016; Astudillo-Defru et al. 2017a,b; Feng et al. 2017; Delisle et al. 2018; Bonfils et al. 2018; Díaz et al. 2019; Zechmeister et al. 2019; Dreizler et al. 2020) and/or that are promising candidates for future atmospheric characterisation (e.g. Bonfils et al. 2018; Díaz et al. 2019).

These discoveries were in large fraction possible thanks to the continuous improvement in instrumentation that provides an

ever increasing precision in the measurement of the radial velocity of the stars. Going from the pioneer ELODIE spectrograph (Baranne et al. 1996), to HARPS (Mayor et al. 2003), SOPHIE (Perruchot et al. 2008; Bouchy et al. 2013), and CARMENES (Quirrenbach et al. 2014), and finally, the ultra-high precision spectrographs such as ESPRESSO (Pepe et al. 2021) and EXPRES (Jurgenson et al. 2016; Blackman et al. 2020), the precision was improved by over two orders of magnitude, attaining now the level of 10 cm s⁻¹.

However, planet detection with these observations are not limited only by instrumental precision, but by intrinsic variability in the star. Even for the least active, slowly-rotating stars, the phenomena collectively called *stellar activity* can produce spurious radial velocity variations with amplitudes of up to a few meters per second, and timescales ranging from a few minutes (pulsations and granulation; e.g. Dumusque et al. 2011b) to decades (activity cycles; e.g. Lovis et al. 2011; Díaz et al. 2016). Particularly worrying are the variations produced by the rotational modulation of the star, as they tend to exhibit power in the same frequency range as some of the most interesting planetary candidates (e.g. Saar & Donahue 1997; Boisse et al. 2009; Dumusque et al. 2011a; Nielsen et al. 2013). The main consequence of the influence of stellar activity is the difficulty to detect exoplanets producing RV variations smaller than 1-ms⁻¹.

Some of the most relevant stellar phenomena that can generate this type of noise are:

Send offprint requests to: L.A Nieto (lnieto@unsam.edu.ar)

1. *Stellar oscillation*: Pressure waves (p-modes) propagate at the surface of solar type stars causing the contraction and expansion of the outer layers over timescales of a few minutes (5–15 min for the Sun, [Broomhall et al. \(2009\)](#); [Schrijver & Zwaan \(2000\)](#)). The radial-velocity signature of these modes typically varies between 10 and 400 cm s⁻¹, depending on the star type and evolutionary stage ([Schrijver & Zwaan 2000](#)).
2. *Granulation*: Various convective motions in the photosphere cause this phenomenon. These *granules*, that emerge from the interior of the star into the photosphere, are hotter than those that cool down and descend. This produces a spurious redshift ([Lefebvre, S. et al. 2008](#); [Dumusque et al. 2011b](#)) that changes depending on the convection pattern and can range from a few minutes to about 48 hours.
3. *Rotational modulation*: The rotation of the star can transport various structures on the surface, causing them to appear and disappear at regular intervals breaking the flux balance between the red-shifted and the blue-shifted halves of the star and creating the illusion of a stellar wobble ([Saar & Donahue 1997](#); [Meunier, N. et al. 2010](#); [Dumusque et al. 2011a](#)).

From a statistical standpoint, one of the main issues is that these phenomena produce correlated error terms, that invalidate some of the most commonly used techniques for planet detection that rely on ordinary least squares, such as the standard periodogram analyses ([Baluev 2008](#); [Zechmeister & Kürster 2009](#)). This problem has often been approached by including correlated noise errors in the modelling of the data. In particular, the use of Gaussian process regression ([Rasmussen & Williams 2005](#)) has been widely adopted by the community (e.g. [Haywood et al. 2014](#); [Rajpaul et al. 2015](#); [Yu et al. 2017](#); [Cloutier et al. 2017](#); [Persson et al. 2018](#); [Bonfils et al. 2018](#); [Díaz et al. 2019](#); [Luque et al. 2019](#); [Suárez Mascareño et al. 2020](#), just to cite a few among a vast body of literature using this technique), fuelled by the availability of specific computer code to perform the necessary calculations effectively ([Foreman-Mackey et al. 2017a](#); [Espinoza et al. 2019](#); [Delisle et al. 2022](#)). However, methods to compare models including this kind of error terms can be time-consuming or unreliable ([Nelson et al. 2020](#)).

A different approach is to bypass the problem of explicitly modelling the effects of activity all together, and rely instead on machine learning models to perform the detection and classification tasks. This has been used mostly for the detection and veto of transiting planet candidates with photometric timeseries (e.g. [Zucker & Gyres 2018](#)), mainly from the space missions *Kepler* (e.g. [Armstrong et al. 2017](#); [Shallue & Vanderburg 2018](#); [Pearson et al. 2018](#); [Ansdell et al. 2018](#)), *K2* (e.g. [Dattilo et al. 2019](#)), or *TESS* (e.g. [Yu et al. 2019](#); [Osborn et al. 2020](#); [Rao et al. 2021](#)), but also from ground-based transit surveys such as the Next Generation Transit Survey (e.g. [McCauliff et al. 2015](#); [Armstrong et al. 2018](#)). These models mostly rely on deep convolutional networks (e.g. [Lecun et al. 1998](#)), that have proven extremely proficient in many fields, mainly computer vision (e.g. [Krizhevsky et al. 2012](#); [He et al. 2016](#)) and natural language processing (e.g. [Peters et al. 2018](#); [Devlin et al. 2019](#)). It is not a surprise that these methods have been advanced mostly for spaced-based photometric surveys, as these missions provide rich datasets that are needed to train this kind of machine learning models. But machine learning has also been employed in the context of exoplanets to study their atmospheres (e.g. [Márquez-Neila et al. 2018](#); [Waldmann 2016](#)), or to classify planets according to their potential habitability (e.g. [Saha et al. 2018](#)). Recently, [de Beurs et al. \(2020\)](#) used neural networks to remove the stel-

lar activity signal from simulated and real RV observations and showed how this can help in exoplanet detection.

In this article, we train a convolutional neural network (CNN) with simulated data to perform the detection of extrasolar planets in radial velocity time series. We frame the question as a classification problem and train the model to distinguish periodograms with and without planetary signals. We show that this method produces better results than the traditional periodogram analyses and correctly identifies more low-mass planets, being also much faster.

2. Planet detection with GLS periodograms

The radial velocity method consists of detecting variations in the line-of-sight projection of the star’s velocity, induced by the presence of an unseen companion.

2.1. Periodograms

Periodograms are often employed to find periodic signals in unevenly sampled time series as those typically obtained in RV surveys. The Lomb-Scargle periodogram ([Zechmeister, M. & Kürster, M. 2009](#); [Khan et al. 2017](#)) has been used extensively to detect periodic signals in RV datasets. In its simplest form, it works in a Fourier-like fashion: the user defines a series of candidate frequencies $\{\omega_i\}$, with $i = 1, \dots, N_f$, and the method fits the radial velocity data, $v(t)$, using a sine-cosine base at the candidate frequency. The better the model at this frequency fits the data (compared to a constant model without variability), the higher the power attributed to the candidate frequency (for details, see [Lomb 1976](#); [Scargle 1982](#); [Baluev 2008](#)). Indeed, the power at frequency ω_i is

$$P(w_i) = \frac{\chi_0^2 - \chi_i^2}{\chi_0^2}, \quad (1)$$

where χ_i^2 is the chi-square statistics for the model at frequency w_i . If we call $f_i(t)$ the model prediction at time t ,

$$\chi_i^2 = \sum_{j=1}^N \frac{(v(t_j) - f_i(t_j))^2}{\sigma_j^2},$$

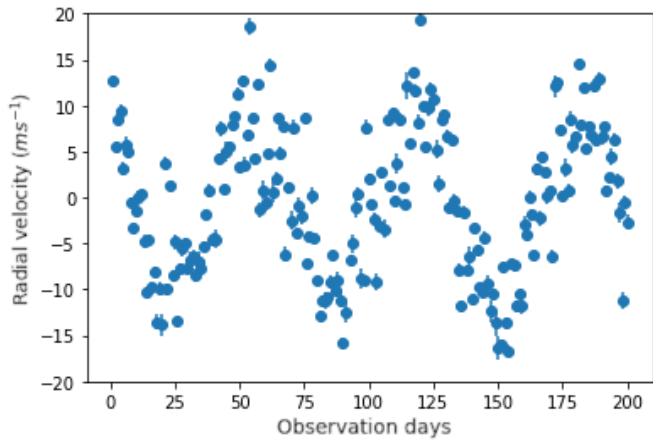
where the sum runs over the N data points in the time series.

A vector is generated with the power of each candidate frequency. The location of the highest power indicates the frequency of a potential periodicity present in the data. Figure 1 shows a time series (with a clear periodic signal) and the resulting periodogram. Note that the width of the peaks expressed in frequency depends solely on the time span of the observations ΔT , and can be expressed

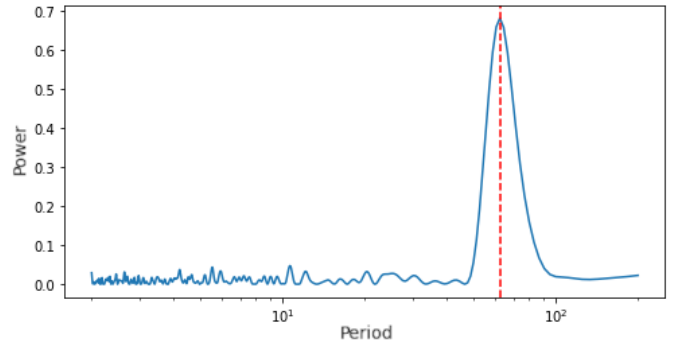
$$\Delta\omega = 1/\Delta T.$$

2.2. False alarm probability (FAP)

Once the periodogram has been constructed, and a candidate period is identified, a tool is needed to help decide whether the observed peak is statistically significant to be considered a periodic signal. This question is traditionally framed as a null-hypothesis significance test, in which the null hypothesis (H_0 , "there is no



(a) Radial velocity measurements.



(b) Periodogram. The red line marks the peak that represents the period with the highest power

Fig. 1: Radial velocity measurements and their periodogram.

planet”) is tested. More precisely, in the analysis of the Lomb-Scargle periodograms, the null hypothesis is often that the observations come from uncorrelated Gaussian noise (i.e., “there is no planet”). The power of the largest peak is used as the test statistics, for which a p -value is computed¹. If the p -value is small enough, then the null hypothesis is rejected. The critical value below which a p -value is considered as evidence for rejecting the null hypothesis is usually between 10^{-3} and 0.1. In many planet search programmes, a FAP value of 0.01 is often used as a threshold below which detected peaks are considered significant (e.g. Howard et al. 2010; Bonfils et al. 2013). In this work, the critical value –which we call FAP_{*} – will be taken as 0.05 with $\log_{10}(FAP_{*})$ rounded to -1.3.

To compute the p -value (FAP) one can take an analytical or numerical approach, using a Monte Carlo algorithm. The analytical expressions (e.g. Scargle 1982; Baluev 2008; VanderPlas 2018) have the advantage of being much faster to compute than Monte Carlo approaches. However, these expressions rely on assumptions and approximations that are only reliable in certain regimes. For example, they often rely on the assumption that the errors are uncorrelated and normally distributed. Following the comments in Baluev (2008) we considered that, if the p -value is greater than or equal to $\log_{10}(0.01)$, the analytical expression is no longer reliable and the other method should be preferred. On the other hand, the Monte Carlo approach samples the data points keeping the observing times and is therefore probably more reliable even for situations where the assumptions on which analytical expressions are based do not hold. In this work, a number of noise realizations are sampled to compute the p -value of the largest peak power with this approach. As we work with simulations, the correct noise distribution is used. This is the most favourable situation which is rarely, if ever, given with real datasets. The Monte Carlo approach requires recomputing hundreds or thousands of periodograms, which makes it a much slower method than the analytical approach, especially when taking into account that we want to analyse a large amount of time series.

As in any null-hypothesis significance test, we are exposed to type I and II errors (e.g. Frodesen et al. 1979). Type I, or “false alarm errors”, occur when H_0 is incorrectly rejected (that is, we

decided a peak is significant when it is not). Type II errors are when we fail to reject H_0 when in fact a planet is present. These errors are also often referred to as false positives and false negatives.

When using this approach, one still needs to decide whether the detected signal is of planetary origin or caused by activity or systematic effects. Often, time series of activity indexes are employed to verify that the candidate frequency is not present in these series, which is regarded as evidence for the planetary interpretation of the signal. However, there is not a universally accepted way to decide whether a signal is produced by a planet.

3. Simulations

To train, validate and test the network a data set of sufficient size is required. In principle, it is not known how large this data set needs to be, but the larger the set with which the network is trained and validated, the better the results it is expected to provide (see Banko & Brill 2001 for a famous example, and the discussion by Halevy et al. 2009).

The data set not only needs to be large but also representative, in terms of number of points, variability, presence of periodic signals, etc., of the cases that the network will encounter when used in “production stage”, i.e. when used to classify actual time series. The available radial velocity time series issued from large scale surveys are too few and too diverse for an efficient training. They do not have enough representatives of each type of variability and planetary system architecture. Besides, not knowing precisely the number of planets in the system means we would also have to deal with the problem of inaccurate labelling, i.e. not being able to precisely convey to the algorithm the class to which a given data set belongs.

The alternative is to train and evaluate the network on synthetic RV time series, and later study its performance on real data sets. If the simulated data are realistic enough, this may be enough, but most probably, an adaptation of the network architecture would be needed. Artificial data have many obvious advantages: being able to produce a large number of time series, and precisely knowing the number of periodic signals in them is fundamental. On the other hand, one clear disadvantage is that the results from our study, at least in principle, will be as relevant as our simulations are realistic.

¹ In the exoplanet literature, this is often referred to as False Alarm Probability (FAP). Although we deem this terminology misleading we will use p -value and FAP interchangeably.

Our network takes periodograms as inputs. We proceed by first generating synthetic time series, from which the Generalised Least-Squared (GLS [Zechmeister & Kürster 2009](#)) periodogram is produced. The reason for this is that while we have relatively good models to simulate time series, the problem of directly simulating periodograms is much tougher. The steps of the simulation process are detailed in the subsections below.

3.1. Time array

The synthetic time series are sampled using 200 quasi-uniformly distributed points. The times are defined by adding random variables drawn from a zero-centred normal distribution with width 0.1 to an evenly spaced time array. Although not completely realistic, this sampling roughly represents an intensive observing season with nightly observations on each target².

3.2. Intrinsic errors

Intrinsic error terms³ are simulated by randomly drawing samples from an uncorrelated multivariate zero-centred normal distribution, with variances informed by the statistics of the uncertainties of the HARPS high-precision survey ([Udry, S. et al. 2019; Díaz, R. F. et al. 2016](#), e.g.). For each simulated star, a star is randomly drawn from the subset of HARPS targets that were observed more than forty times by the survey. Using the observations of this star, the mean velocity uncertainty, $\bar{\sigma}_v$, is computed. Then, 200 samples are drawn from a normal distribution centred on $\bar{\sigma}_v$ and with a width of 0.30 ms^{-1} , which is a typical value for the dispersion in the velocity uncertainties of observed stars. Negative values are replaced by $0.5\bar{\sigma}_v$. In this way, each data point has a slightly different uncertainty and error term, as is usually the case in real time series.

3.3. Activity signals

It has already been mentioned that there are several components of stellar noise that can alter radial velocity measurements. Simulated effects of pulsations and granulations were based on the work by [Dumusque et al. \(2011b\)](#). The authors studied the power spectrum of five well-observed solar stars, the spectrum is fitted with a Lorentzian component that represents the pulsations and three components for the granulation, mesogranulation and supergranulation. Using the fitted parameters defined in there, the power spectrum is constructed as the sum of these four components, with randomly chosen phases for each component. The resulting power spectrum is used to generate the synthetic radial velocity measurements.

The effect of the rotational modulation was simulated using samples from a Gaussian process with a covariance function generated with the pseudo periodic kernel:

$$k_{QP}(t_i, t_j) = A^2 \exp\left(-\frac{(t_i - t_j)^2}{2\tau^2} - \frac{2}{\epsilon} \sin^2\left(\frac{\pi(t_i - t_j)}{\mathcal{P}}\right)\right)$$

This *kernel* is used widely in the exoplanet literature to model this kind of effect⁴ and has been used to infer the rotational period and other parameters of astrophysical interest related to stellar activity and rotation (e.g. [Giles et al. 2017; Angus et al. 2018](#)) This *kernel* has 4 hyperparameters: A , the covariance amplitude; \mathcal{P} , the recurrence time, which would be given by the rotation period; τ , the decay time, associated with the average lifetime of an active region; ϵ , the structure factor, a parameter associated with the number of active regions that occur simultaneously.

To define the values of these hyperparameters for each simulated time series we resorted again to the HARPS survey. All stars in the survey have an estimate of their rotation period obtained from a measurement of their magnetic activity using the calibration by [Mamajek & Hillenbrand \(2008\)](#). For each simulated velocity series, the value of \mathcal{P} was randomly chosen from the sample of estimated rotational periods for HARPS stars. The remaining parameter values were sampled from distributions:

$$\begin{aligned} A &\sim \text{gamma distribution, } \Gamma(2.0, 0.5). \\ \tau &\sim \text{normal distribution, } \mathcal{N}(3 * \mathcal{P}, 0.1 * \mathcal{P}). \\ \epsilon &\sim \text{uniform distribution, } \mathcal{U}(0.5, 1.0). \end{aligned}$$

Adding the intrinsic errors to the activity signals makes the time series of radial velocities without a planet rv_{wp} .

3.4. Planets

The contribution of planets to the velocity time series is generated assuming circular orbits. Additionally, we disregard mutual interaction in multi-planetary systems.

Therefore, we need three parameters: the orbital period, P_{pl} , the semi-amplitude of the variation K , and the time in which the variation is zero, T_0 . The value of P_{pl} was chosen randomly between $10 * \delta$ and $\Delta_t/2$, where δ is the minimum distance between two points in the time series, and Δ_t is the total duration of the series. The value of K was drawn from a log-uniform distribution between 0.1 ms^{-1} and 10 ms^{-1} . Finally, T_0 was randomly chosen as a moment within an orbital period.

The variation then takes the form:

$$rv_{pl} = K \sin\left(\frac{2\pi(t - T_0)}{P_{pl}}\right)$$

Once the vector rv_{pl} has been obtained, it was added directly to rv_{wp} to get the time series with planet (see figure 2).

In line with our decision to neglect mutual interactions, to model multi-planetary systems, the procedure is repeated for each planet and the contributions were added.

3.5. Periodograms

GLS periodograms were computed for each simulated time series on a grid of uniformly-sampled orbital frequencies, between δ_v and 0.5 d^{-1} , with a constant step of $\delta_v/10$ (i.e. using an over-sampling factor of ten), where δ_v is the inverse of the duration of the time series:

$$\delta_v = \frac{1}{\max(t) - \min(t)}$$

⁴ See references in the Introduction for a number of examples of articles using Gaussian Processes with this kernel.

² The sampling may be seen as done in sidereal days

³ Here we call error terms to the unknown term that makes the observed velocities deviate from the model. In contrast, the term uncertainties is reserved to the experimental error associated with each measurement.

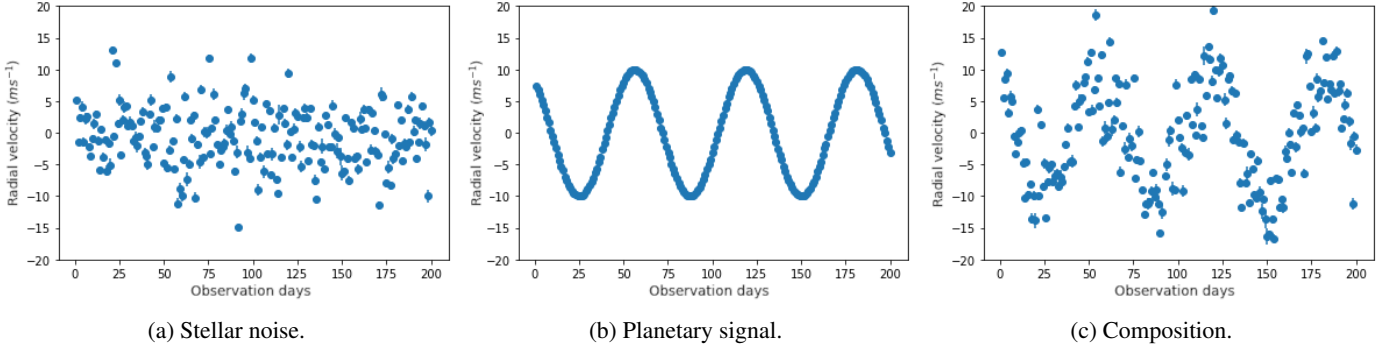


Fig. 2: Composition of stellar noise with a planetary signal with a period of 62 days and an amplitude of 10ms^{-1} .

3.6. Datasets

To train, validate and test the neural network, several datasets are needed to guarantee the robustness of the proposed solution and the quality of the results.

The usual methodology when working with periodograms is to analyze the maximum peak and define if it comes from a significant signal. If it is the case, the signal is removed from the original time series, and a new periodogram is generated using the model residuals, where a new maximum peak is identified and analysed in a similar fashion. This means that the network will not only receive the original periodogram as input, but also subsequent periodograms obtained in this manner. So, in addition to simulating periodograms of stars with up to four planets, we also constructed additional periodograms by removing the signal at the largest peak frequency (regardless of whether it was significant or not). This process was performed four times for each original signal. This not only serves to have more varied periodograms, but also increases the size of the training data.

This particular type of problem where an input is considered and has to be assigned to one of two classes (here, planet or not planet) is called a binary classification problem. In this type of problem, it is very important to consider the balance of the classes in the data set –i.e. the fraction of instances from each case– and the metrics used during training. For example, if an algorithm is trained with many more cases of a given class, it may be biased against predicting the minority class. This may lead to a model with a relatively good accuracy (i.e. the fraction of cases correctly classified), but ultimately useless.

This was considered when constructing the training, validation, and test sets. The first two were for training and parameter adjustment, and the final one was for testing the complete method. For all the sets the same number of stars with 0, 1, 2, 3, and 4 planets were generated and all their periodograms, constructed as described above, were used for parameter tuning and testing. Due to the nature of the generation process, these sets are naturally unbalanced toward negative cases. Consider that from each system, four periodograms are generated independently of the number of planetary signals injected. Then, for each star without planets, for example, four periodograms with negative labels will be produced. In addition, for systems with planets, it may occur that the planetary frequency is not at the maximum peak, which would lead to another negative label, even in the presence of a planet in the simulation. This was not considered a problem for data sets used for evaluation because they are seen as a realistic application. For the training set, however, a balanced data set is more important, periodograms were randomly selected to have near half-positive and half-negative cases.

In summary, three data sets were generated. In all cases, we simulated an equal number of stars with 0, 1, 2, 3, and 4 planets.

- *Set 1 - 3425 stars*: from which 13700 periodograms were generated with the process described above. This set was balanced by randomly selecting positive and negative cases until 40% of positives cases was reached. This set was used for train and validation (see Sect. 4).
- *Set 2 - 2550 stars*: from which we get 10000 periodograms. This set was used for comparisons between methods and threshold search (see Sects. 5.1 and 5.2).
- *Set 3 - 5000 stars*: which lead to 20000 periodograms. It was used to apply the *Virtual Astronomer* to each star and to analyze the distribution of output values for the FAP and the CNN (see Sects. 5.3 and 5.5).

4. Convolutional Neural Network

The neural network (nicknamed ExoplanNET) was implemented using the Keras package for python, with Tensorflow as backend. It receives one GLS periodogram, represented in a one-dimensional array of data, together with two additional characteristics: the power and position of the largest peak in the 1D array. The input GLS periodogram was sampled in a grid of 990 frequencies. The frequency grid was fixed and was the same for all simulated velocity datasets. The output is a single value representing the probability that the data was originally created from a periodic signal (in addition to the activity signals).

A natural solution in this setting is to use convolutional networks in one dimension.⁵ The architecture is quite standard. The hidden layers will be composed of convolutional layers, interleaved with max pooling layers. Finally, a series of dense layers are implemented, interspersed in turn with dropout layers. All layers use ReLU activation functions except the output neuron which uses a sigmoid activation function for classification that returns a real value between 0 and 1.

The network is trained using the cross-entropy loss function,

$$E = \sum_{i=1}^N [t_i \log(p_i) + (1 - t_i) \log(1 - p_i)] ,$$

where the sum is over all the instances (of a batch) of the dataset, p_i is the predicted probability of belonging to the positive class, and t_i is the target variable (1 if the data contains a periodic signal; 0 otherwise). In each training epoch the dataset is divided

⁵ In section A there is a brief explanation of this type of network and its use in data that have a spatial relationship, such as images or periodograms.

in batches of 128 periodograms, and the weights (parameters) of the model are adjusted using the Adam optimizer, with gradients computed based on the partial loss function. This is standard procedure in machine learning literature and has been shown to increase the performance and convergence of the optimization process (see, for example, Bishop 2007).

The evolution of the training was monitored using the *F-measure* (or F-score), which is the harmonic mean of precision (*P*) and recall (*R*), $F_1 = 2(PR)/(P + R)$. In turn, precision and recall are defined:

- *Precision*: is the ratio of *true* positive cases among those that were *marked* as positive. In our case it would be:

$$P = \frac{|\{\text{Real planets}\} \cap \{\text{Marked as planet}\}|}{|\{\text{Marked as planet}\}|}$$

- *Recall*: It is the ratio of *true* positive cases detected among the positive *existing*.

$$R = \frac{|\{\text{Real planets}\} \cap \{\text{Marked as planet}\}|}{|\{\text{Real planets}\}|}$$

Unlike the *accuracy*, the F-score is appropriate even in unbalanced cases.

Different network configurations were tested and evaluated with the validation set. The final architecture achieved an F-score of 0.88 in the validation set. A diagram of retained architecture is shown in figure 3. The trained network is provided in h5 format in a GitHub repository⁶, together with a sample of labelled periodograms for testing.

5. Results

5.1. Predictive performance

For a given periodogram, both the classical FAP computation and our CNN output a number. In the former, it is the log probability that a peak with at least as much power as the largest peak observed in the periodogram appears under the null hypothesis (i.e. only noise –albeit correlated– is present in the time series). In the latter, it is a value between 0 and 1 that can be interpreted as the probability that the periodogram contains a *bona fide* planetary signal. Both implementations require the definition of a threshold value if they are to be used for taking decisions, such as defining whether a planet is present in the data or not. However, note that the FAP method is only intended to assess the significance of a signal, while the neural network also aims at providing a classification of the nature of the signal.

Before setting this threshold, an analysis of the overall effectiveness of each method can be made and compared with each other, using *precision-recall* curves. From the definitions seen in the previous section, it is trivial to see that both metrics vary between 0 and 1, the intuition behind precision is that it seeks to minimize false positives and recall does so with false negatives.

The precision-recall (PR) curve (Fig. 4) shows the tradeoff between these metrics. This curves are constructed by varying the threshold for detection and computing the metrics at each value. Ideally, the curves should pass as close as possible to the upper right edge of the plot, that represents a system with perfect recall and no false positives. Therefore, the greater the area under this curve, the better the overall performance of the algorithm. The area under the curve of the PR curve (PR-AUC) is useful to compare two different solutions to the same problem.

⁶ <https://github.com/nicklessagus/ExoplaNNet>

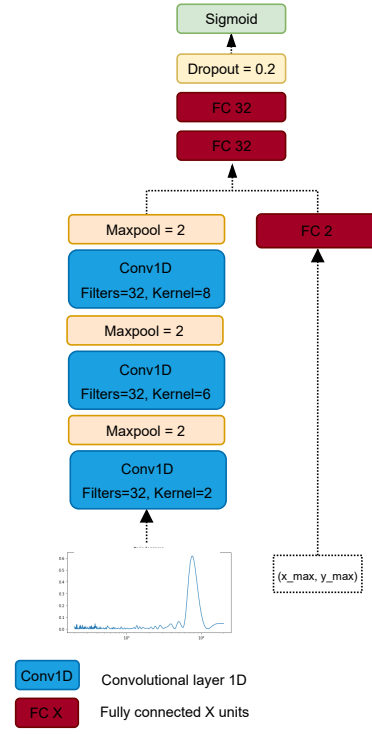


Fig. 3: Architecture of the ExoplaNNet neural network. Blue cells represent convolutional layers; pale orange cells are Max-Pooling layers, and dark red cells are fully connected layers. In addition, we show the single DropOut layer in yellow and the output layer in green.

In Figure 4 we present the PR curve and PR-AUC metric for the classical FAP method over the periodograms of *set 2*. We see that the network performs systematically better than the traditional method. The AUC metrics are 0.90 and 0.96 for the FAP and ExoplaNNet methods, respectively.

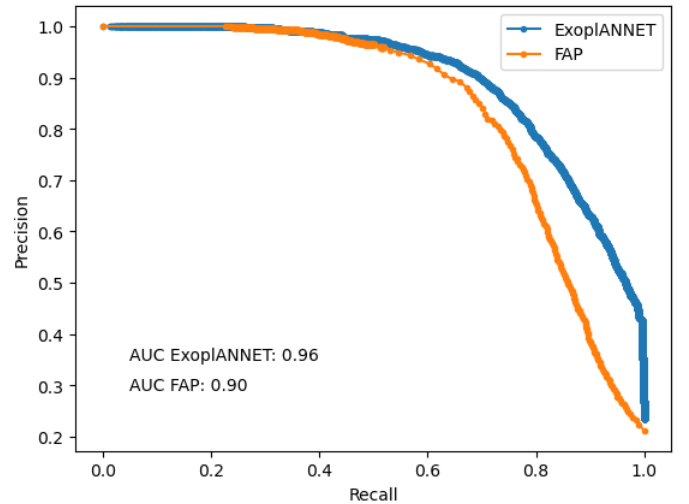


Fig. 4: Precision-Recall Curve and AUC of both methods over the periodograms of *set 2*.

In Figure 5 we present the distribution of the output values (i.e. FAP values and planet probability) for the periodograms of *set 2*. As expected, periodograms for which the methods assign a

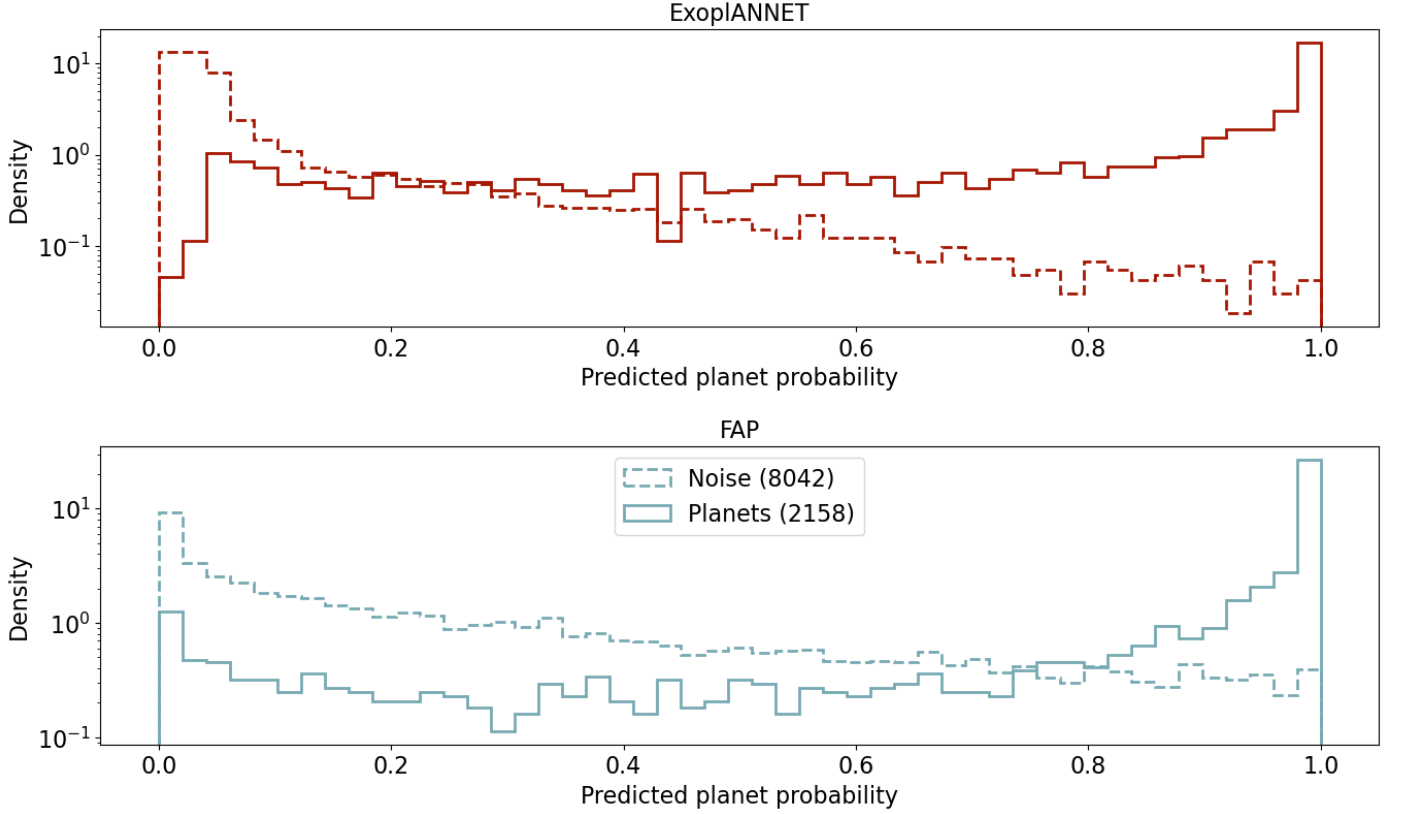


Fig. 5: Distribution of output values over the periodograms of set 2 (probabilities and FAP values for the CNN and classical analysis, respectively). For each algorithm the distribution of data labelled as planets and as noise are shown with different line styles. As there are 15587 periodograms without planets for the 4413 planetary periodograms, the distributions are normalised for easier comparison.

probability close to 1 are predominately originated by real planets. Inversely, outputs very close to zero are mostly associated with periodograms containing no planets. On the other hand, the value of the x-axis where both histograms cross is much larger for the FAP method.

5.2. Defining the Threshold for planet detection

Once the general performance has been analyzed, we now turn to the topic of finding an adequate threshold for the neural network model. As was already mentioned we considered a log threshold of -1.3, i.e. a 0.05 probability for the FAP. The number of false positives and false negatives produced by the FAP method using this threshold were computed, and used to find the range of probability thresholds for the network that give a smaller number of both false positives and false negatives.

In Figure 6, the number of false positives and false negatives are shown as a function of the threshold used for the network. The values produced by the FAP method are marked as horizontal dashed lines. This defines a range between 0.69 and 0.77 within which the network obtains better results than the FAP. Any threshold value greater than 0.69 will give fewer false positives, and those less than 0.77 will give fewer false negatives. The network threshold was then set to 0.77, in order to produce the most reliable detection mechanism in terms of false positives, with a similar recall as the traditional method.

		Prediction	
		0	1
Real Value	0	15309	277
	1	1672	2742

(a) Confusion matrix FAP

		Prediction	
		0	1
Real Value	0	15388	198
	1	1674	2740

(b) Confusion matrix Exop1ANNET.

Table 1: Confusion matrices Exop1ANNET and FAP. The rows show the true labels of positive and negative cases in the set and the columns show the predicted label

5.3. Performance on test set

The last performance evaluation was conducted on set 3. Since set 2 was used to identify the threshold range where the network performs better than the traditional method, there is a concern that the choice of the threshold may have been influenced by the characteristics of this particular set, leading to overfitting. To address this, we evaluated the network's performance on the yet-unseen set 3.

The *confusion matrices* for both methods are shown in tables 1a and 1b. The rows show the true labels of positive and negative cases in the set and the columns show the predicted label.

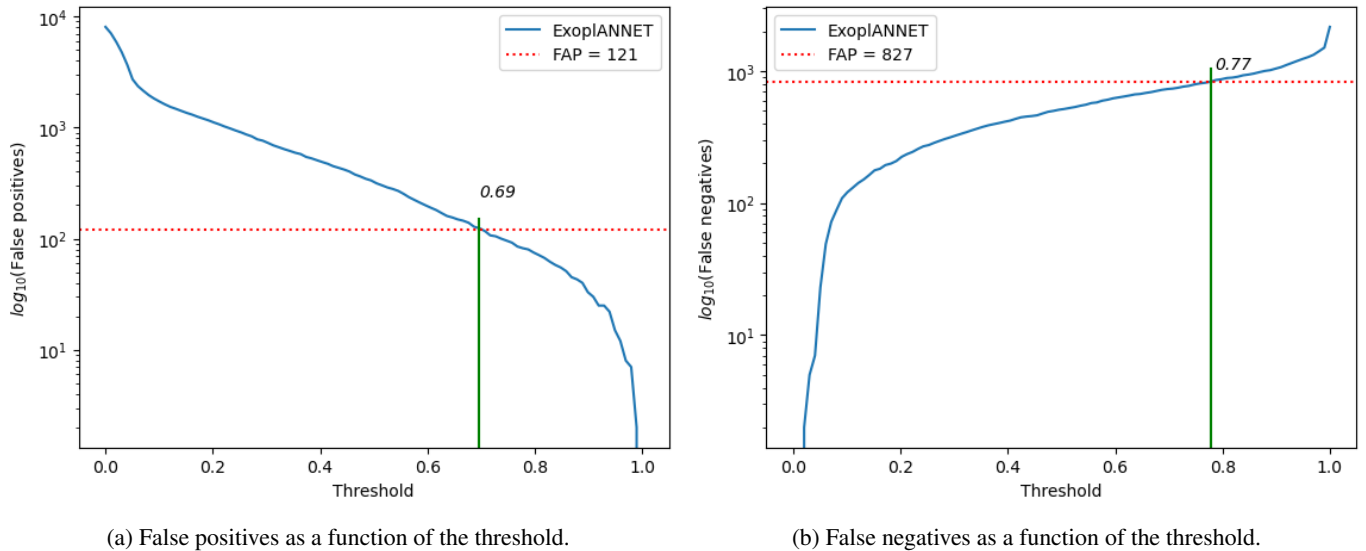


Fig. 6: Lower and upper limit of the threshold where the network has both fewer false positives and false negatives than the traditional method. The dashed horizontal lines show the number of wrong detections with the FAP method, and the vertical segment aids in the identification of the corresponding probability threshold.

The results obtained in this evaluation are consistent with those from set 2. Compared to the traditional method, the number of false positives is decreased by 28.5%, while only two additional false negatives were identified. This is reflected in the comparison in table 2, where the recall remains almost unchanged but the precision is increased.

	FAP	ExoplaNNet
Precision	0.908	0.932
Recall	0.621	0.620

Table 2: ExoplaNNet and FAP Precision/Recall.

5.4. Execution time

It was shown in the introduction that, depending on the result, the calculation of the FAP can be done using the Baluev formula or by a Monte Carlo-type algorithm. The analytical formula is not very computationally expensive but assumes white noise. On the other hand, running the Monte Carlo computation on a large data set of radial velocities and computing their corresponding periodograms can take up considerable time, specially when red noise has to be simulated. All this means that the average time required to calculate a FAP value can be considerable.

The case of the network is quite different. A trained network is nothing more than a large matrix and making a prediction is simply taking the input and executing basic operations such as addition and multiplication to return a value. Because of this simple fact, the network should be much faster⁷.

To compare the execution times between the methods, we need to consider the *Wall-Time* and the *Proc-Time*. The latter is the time used exclusively to execute a process. It does not take into account things like disk access or other input/output operations, operating system interruptions, time used in other processes, etc. In contrast, *Wall-Time* is the clock time it takes to execute something. It is simply a stopwatch, so if the process

is waiting to read data or the system is very busy with several processes, it will add to this time.

On the other hand, if you want to evaluate the time of small programs or pieces of code, it is usually convenient to see only the *proc-time*. The code for generating the periodograms is not parallel (at least not in its current implementation), so these two times should be very similar.

The methods were executed several times, and the resulting running times were averaged. For the FAP method, we perform 100 executions (note that if Baluev's result is good enough, the Monte Carlo simulations are not necessary). For the network method, we generated predictions for 10^6 periodograms⁸. The results are presented in table 3 where we report the time taken to analyse a single periodogram, expressed in seconds.

	FAP	ExoplaNNet
<i>Wall-Time</i>	425.97 s	0.0011 s
<i>Proc-Time</i>	427.69 s	0.0034 s

Table 3: Execution times in seconds for the analysis of a single periodogram with ExoplaNNet and FAP methods.

The difference is considerable. Focusing only on *proc-time*, the network is 125,791 times faster, that is, a difference of 5 orders of magnitude. The execution time required to calculate the FAP can seem excessively long, but we remind the reader that the Monte Carlo simulations performed include red noise, in an attempt to make the method as reliable as possible.

Note however that the code to calculate the FAP is not optimized. The noise simulations and the computation of the periodograms are severely affecting performance. These parts of the computation could be optimized, and the Monte Carlo procedure could be parallelized. However, the reality is that the advantage that the network brings is too great for any realistic optimization to bring it even close to these results.

⁷ Just to mention another advantage, the network occupies only 1.7kB in memory.

⁸ The executions were on a desktop computer with a 2.3 GHz micro Intel Core i5 with 8Gb of RAM.

5.5. Virtual Astronomer

Having compared the performance of ExoplanNET with the traditional method using the FAP, we now seek to compare how both implementations would work in the full process of sequentially finding planets in a time series.

The procedure often follows these lines: when a significant peak is found (i.e. its $\log_{10}(FAP) \leq -1.3$), a sinusoidal signal at that frequency is fit and removed from the data. A new periodogram is computed from the residuals, and the process is repeated until the largest peak in a periodogram is not deemed significant. The pseudocode of this procedure –called *virtual astronomer*– is shown in Algorithm 1. This procedure is often the first step in analysing a radial velocity time series, although there are much more sophisticated techniques to evaluate the significance of a signal in a dataset (e.g. Díaz, R. F. et al. 2016).

Algorithm 1 virtual astronomer

```

1: procedure VIRT_ASTRO( $rad\_vel$ )
2:    $pg \leftarrow \text{gen\_periodogram}(rad\_vel)$ 
3:    $max\_peak \leftarrow \text{get\_max\_peak}(pg)$ 
4:    $planets = []$ 
5:   while planet( $max\_peak, pg$ ) do
6:      $planets.append(max\_peak)$ 
7:      $new\_rad\_vel \leftarrow \text{remove}(max\_peak, rad\_vel)$ 
8:      $pg \leftarrow \text{gen\_periodogram}(new\_rad\_vel)$ 
9:      $max\_peak \leftarrow \text{get\_max\_peak}(pg)$ 
10:  return  $planets$ 

```

So far, all the tests were performed on individual periodograms, which may have contained any number of simulated planets between zero and four, but how the methods behave when used as part of the *virtual astronomer* was not studied.

We performed an analysis using the threshold values determined in the previous section. Both implementations of the *virtual astronomer*, one using the classical FAP computation and another one using the CNN predictions, were applied to each of the 5000 stars in the third data set. The idea is to test how many planets the methods actually find in a complete, more realistic use case. In particular, we are interested in exploring their behaviour with respect to false positives.

While it is clear from the above analysis that ExoplanNET performs better in terms of false positives, it is not so clear that this would also be the case when using it with the *virtual astronomer*. On the one hand the *virtual astronomer* with the FAP method labels more noise peaks as planets, which means that on average the execution will proceed over more iterations than the implementation using ExoplanNET. This may increase the chances that in those additional iterations, the method detects planets that ExoplanNET could not find because it was better at identifying the first dominant non-planetary peak, which stopped of the algorithm. On the other hand, this could also mean more false positives are identified with the FAP method.

To evaluate the performance of the *virtual astronomer* using each detection method, the numbers of false negatives and false positives were compared. In figure 7 we compare the performances as a function of the actual number of planets in the simulated system. The *virtual astronomer* using ExoplanNET yields a lower number of false positives, compared to the implementation with the FAP method. Additionally, the number remains approximately constant over systems with different number of planets (7). On the other hand, the results using the FAP exhibit a larger difference for stars with different number of planets.

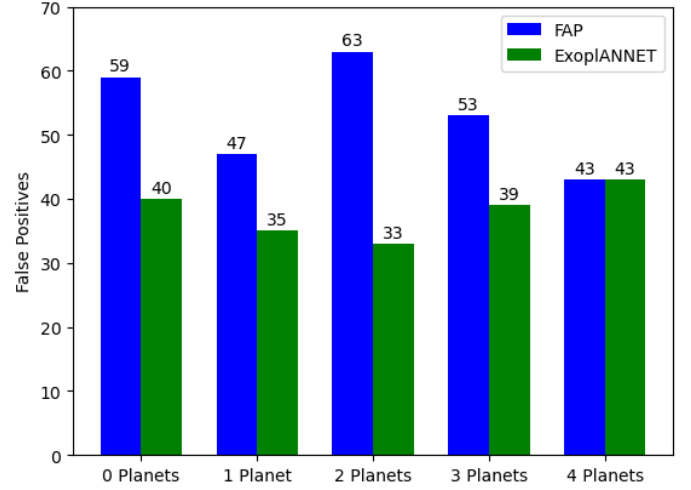


Fig. 7: False positives of the *virtual astronomer* with both implementations.

To further evaluate both implementations, the numbers of detected planets were compared to the maximum possible number under flawless decision making, i.e. the maximum number of planets that could be found by the *virtual astronomer* if it had access to the real labels of the peaks. Remember that the fact that a star has N planets does not mean that all those planets will be reached by the *virtual astronomer*. If at a given step the peak corresponding to the planet is not the largest peak in the periodogram, the *virtual astronomer* will fail to identify it, and the process will stop. The results are shown in Figure 8.

In general, the *virtual astronomer* using the FAP method permits detecting more planets in the system. However, these extra planets come at the price of a larger number of false positives (Fig. 7). Similarly, the *virtual astronomer* using the FAP method exhibits systematically less false negatives, but only by a very small amount. Also, with the exception of the data with four planets, the FAP methods also has less missed planets, i.e. planets that are not even evaluated by the method. This was expected because of the larger number of iterations brought forth by a larger false positive rate. Overall, the FAP method is more inclined to provide a positive classification, which brings more planets but also more false positives.

Finally, to provide a global view, we computed the accuracy and completeness metrics of each implementation (see Table 4). Despite the difference in the number of periodogram evaluations with each implementation, the precision and completeness values maintain the relationship they had when they were based on single periodogram evaluations. Globally, the completeness is almost the same but the implementation with ExoplanNET increases the precision of the results, significantly reducing the number of false positives.

	Virtual Astronomer FAP	Virtual Astronomer Red
Precision	0.911	0.934
Recall	0.747	0.741

Table 4: Precision and Recall of the *Virtual Astronomer*

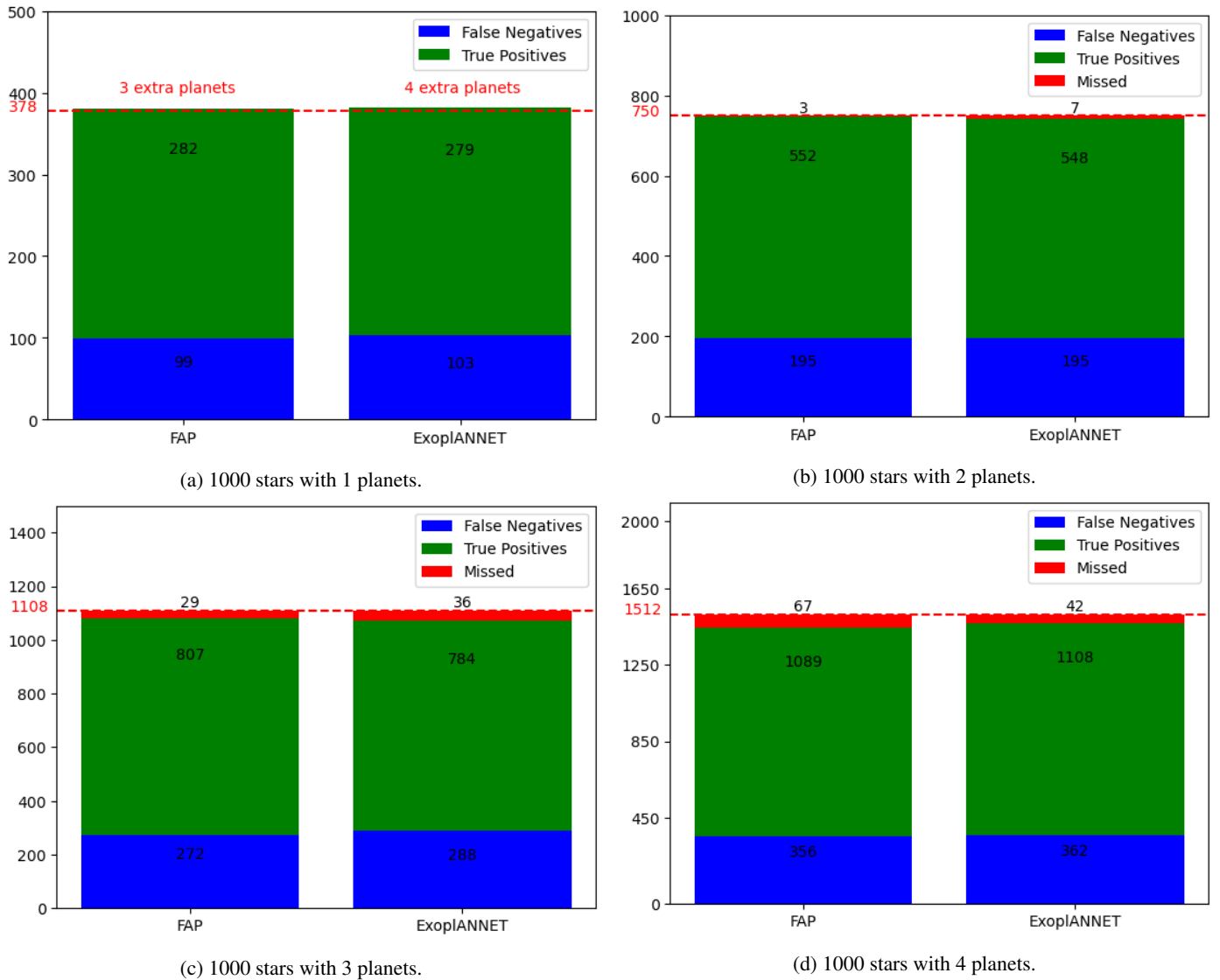


Fig. 8: Detections of both implementations of the *virtual astronomer*, compared to the detections provided by the optimal method. The number of planets detected by the optimal method is marked by a dashed line and indicated in red on the vertical axis. Each panel corresponds to systems with a given number of companions. The bars present the true positive (i.e. detected planets, green), false negatives (blue) and planets that were not detected (i.e. their peak was not evaluated) whereas the optimal *virtual astronomer* does. Note that even using the optimal method, many planets are missed; the numbers of planets present are much larger than the number of detected planets, even with the optimal method.

6. Discussion

Having analyzed the general behaviour of the FAP and ExoplaNNet as methods for identifying *bona fide* planets in the presence of correlated noise, we now turn to explore the dependence of the performance of the methods with planetary parameters.

In Figure 9 we plot the precision and recall metrics as a function of the periods of the signals identified as planets, binned every five days. Both methods lose precision in the period range between 30 and 60 days. But while the precision of the FAP method drops below 0.75, the precision of ExoplaNNet predictions stays above 0.85. On the other hand, the FAP shows a relatively constant recall across orbital periods, while the network exhibits a clear decrease at around the same period range.

This period range is associated with stellar rotation, and therefore many false positive signals are expected to appear here.

Our interpretation is that ExoplaNNet learns to be more “cautious” when labelling peaks appearing in this range, which incidentally is the same way a professional astronomer usually behaves. As a consequence, the recall is degraded but the precision is kept relatively high. The FAP, on the other hand, does not exhibit any dependence in recall with orbital period and is therefore labelling more noise peaks as planets. As a consequence, the precision is degraded even more than for the network.

In Figure 10 precision and recall are plotted as a function of the periodogram peak powers, binned every 10 units of relative power. Although the curves for both methods are similar, for low-power peaks ExoplaNNet is more precise. This leads us to think that the network must be considering characteristics of the periodogram other than the maximum peak power, which allows it to better identify the relatively faint planetary peaks. It is in this range where the network produces less false detection

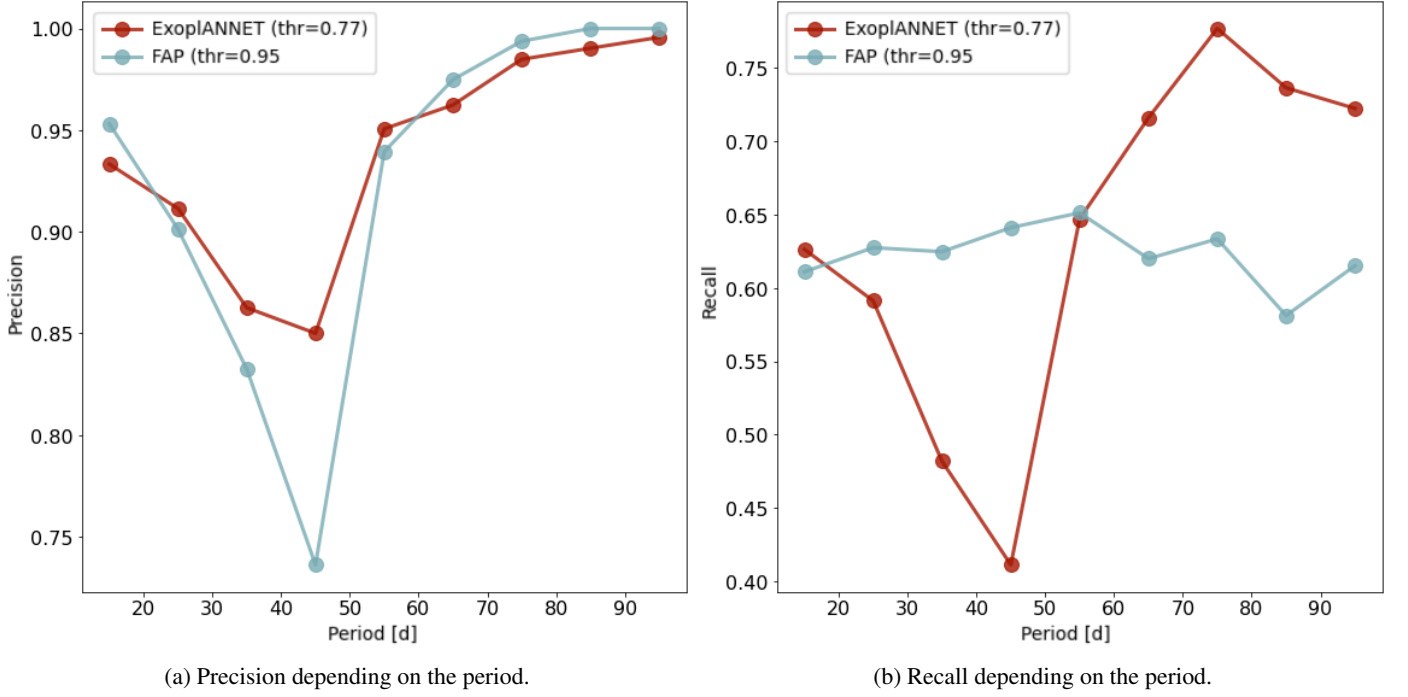


Fig. 9: Precision and recall as a function of the period of the detected planets, using the threshold (thr) 0.77 for the network and 0.95 for the FAP (see Sect. 5.2).

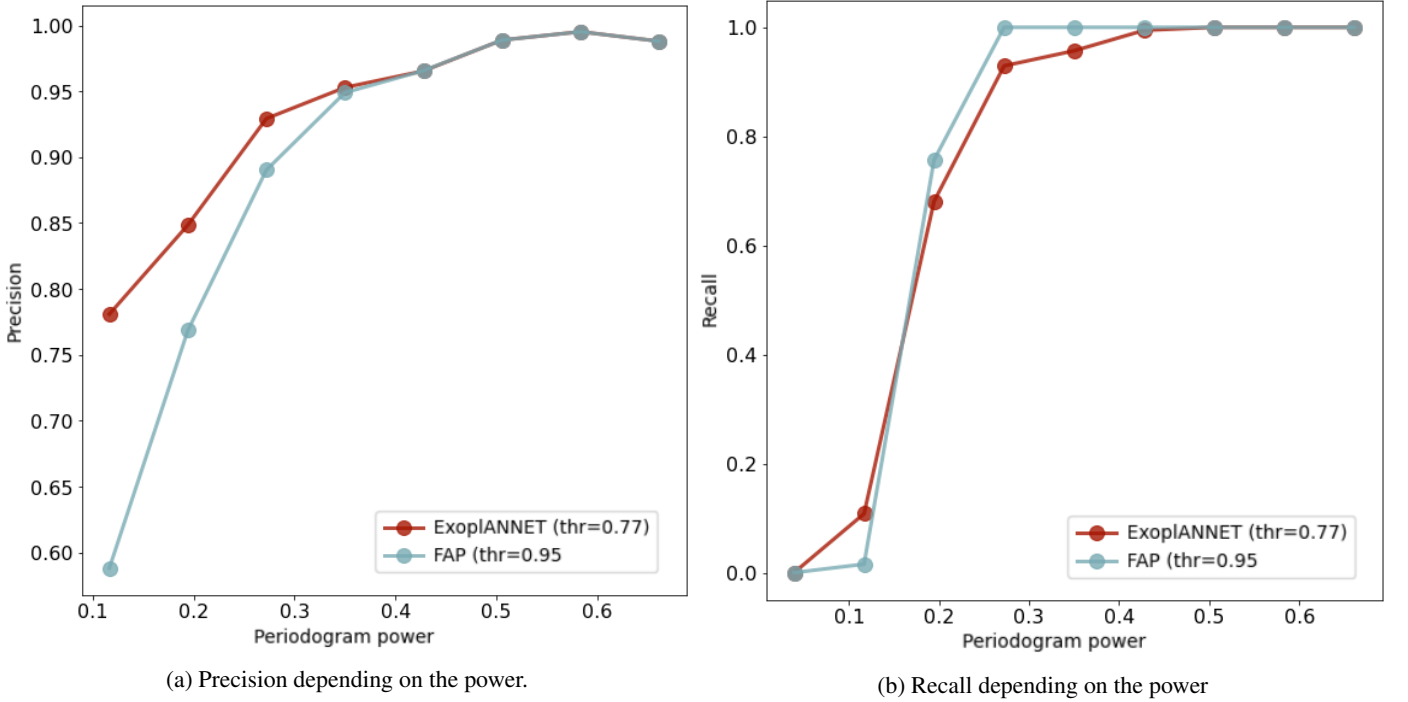


Fig. 10: Precision and recall as a function of the power in the periodogram of the detected planets, using the threshold (thr) 0.77 for the network and 0.95 for the FAP.

than the FAP method, which explains the results of the previous sections.

7. Conclusions

We implemented a Convolutional Neural Network model (named ExoplanNET) to evaluate the presence of planetary sig-

nals in radial velocity periodograms. The algorithm was trained on simulated data including red noise and various planetary companions. Its performance was evaluated using previously unseen data and compared with the traditional method based on null hypothesis significance testing, a.k.a. false alarm probability (FAP).

Our method outperforms the FAP method on single periodograms, as evaluated by the precision-recall area-under-curve metrics. In other words, a threshold can be chosen, so that it produces a similar level of recall with about 30% less false positives. In addition, the network is at least five orders of magnitude faster than the traditional FAP method. However, remember that in this work, the noise realizations used to compute the significance of observed peaks are performed using correlated noise, which is certainly slower than methods using only white noise, and could in addition be further optimised by using dedicated methods (e.g. Foreman-Mackey et al. 2017b; Ambikasaran et al. 2015). Finally, ExoplaNNet employs barely 1.7kB of computer memory. The trained network is provided in h5 format in the repository <https://github.com/nicklessagus/ExoplaNNet>, together with a sample of labelled periodograms for testing.

The detection method was implemented within an iterative procedure to sequentially explore the presence of planetary signals in a radial velocity data set. This “virtual astronomer” evaluates the maximum peak present in a given periodogram and if it decides it belongs to a planet removes a sinusoidal signal at the detected period and proceeds using the model residuals. If a peak is classified as not belonging to a planet, the procedure stops. The FAP method was again used as comparison for the performance of ExoplaNNet used as part of the virtual astronomer. Overall, our new method exhibits a better precision metric than the FAP (0.93 vs. 0.91), while keeping a similar recall metric.

However, using the virtual astronomer with the FAP method more planets are detected, at the expense of a larger number of false positives. It is probably the higher false positive rate that allows the virtual astronomer with the FAP method to evaluate periodograms which follow from a false detection. The same periodogram might be ignored by the virtual astronomer using the ExoplaNNet model if the first peak was correctly identified as noise. Indeed, we see that the number of missed planets (i.e. planets that are not even evaluated by the algorithm) is larger under ExoplaNNet.

The behaviour of the detection metrics as a function of the period of the signal being detected shows a qualitative difference between ExoplaNNet and the traditional FAP method. While the FAP retains a relatively constant recall across the entire period range, the neural network seems to have learnt to be more cautious in the period range associated with stellar rotation –and hence activity. As a consequence, while both methods lose precision at this period range, ExoplaNNet’s precision remains larger than the one computed with the FAP. This is precisely the reason implementations using machine learning algorithms are useful. As mentioned in the Introduction, the objective is to bypass the modelling of the stellar activity and being able to distinguish between bona fide planets and spurious RV signals nevertheless. In this sense, the comparison with the FAP method is unfair: the traditional method is not even intended to distinguish activity from planets, but merely to claim statistical significance of a signal. Our machine learning method is therefore producing two results at the same time: assessing the significance of a signal and identifying its nature.

Future work shall focus on evaluating the performance on real time series, both by performing simulations with realistic time sampling, and on actual observed data. In addition, neural networks can be provided with rich context to the classification task in the form of additional data. In our case, ExoplaNNet takes the position and power of the largest peak in the periodogram. Additional information can come in the form of the stellar rotational period and spectral type, for example. Imple-

menting and exploring these possibilities will constitute avenues for future advancement.

Acknowledgements. Part of this work was carried out at the Geneva observatory and financed by the Seed Money project Grant 2018 “Towards the Detection of Earth Analogues (TDEA)” of the STATE SECRETARIAT FOR EDUCATION, RESEARCH AND INNOVATION, Switzerland.

References

- Ambikasaran, S., Foreman-Mackey, D., Greengard, L., Hogg, D. W., & O’Neil, M. 2015, *IEEE Transactions on Pattern Analysis and Machine Intelligence*, 38, 252
- Anglada-Escudé, G., Amado, P. J., Barnes, J., et al. 2016, *Nature*, 536, 437
- Angus, R., Morton, T., Aigrain, S., Foreman-Mackey, D., & Rajpaul, V. 2018, *MNRAS*, 474, 2094
- Ansdell, M., Ioannou, Y., Osborn, H. P., et al. 2018, *ApJ*, 869, L7
- Armstrong, D. J., Günther, M. N., McCormac, J., et al. 2018, *MNRAS*, 478, 4225
- Armstrong, D. J., Pollacco, D., & Santerne, A. 2017, *MNRAS*, 465, 2634
- Astudillo-Defru, N., Díaz, R. F., Bonfils, X., et al. 2017a, *A&A*, 605, L11
- Astudillo-Defru, N., Forveille, T., Bonfils, X., et al. 2017b, *A&A*, 602, A88
- Balcev, R. V. 2008, *Monthly Notices of the Royal Astronomical Society*, 385, 1279
- Banko, M. & Brill, E. 2001, in *Proceedings of the 39th Annual Meeting on Association for Computational Linguistics*, ACL ’01 (USA: Association for Computational Linguistics), 26–33
- Baranne, A., Queloz, D., Mayor, M., et al. 1996, *A&AS*, 119, 373
- Bishop, C. M. 2007, *Pattern Recognition and Machine Learning* (Information Science and Statistics), 1st edn. (Springer)
- Blackman, R. T., Fischer, D. A., Jurgenson, C. A., et al. 2020, *AJ*, 159, 238
- Boisse, I., Moutou, C., Vidal-Madjar, A., et al. 2009, *A&A*, 495, 959
- Bonfils, X., Astudillo-Defru, N., Díaz, R., et al. 2018, *A&A*, 613, A25
- Bonfils, X., Delfosse, X., Udry, S., et al. 2013, *A&A*, 549, A109
- Bouchy, F., Díaz, R. F., Hébrard, G., et al. 2013, *A&A*, 549, A49
- Broomhall, A.-M., Chaplin, W. J., Davies, G. R., et al. 2009, *Monthly Notices of the Royal Astronomical Society: Letters*, 396, L100
- Cloutier, R., Astudillo-Defru, N., Doyon, R., et al. 2017, *A&A*, 608, A35
- Dattilo, A., Vanderburg, A., Shallue, C. J., et al. 2019, *AJ*, 157, 169
- de Beurs, Z. L., Vanderburg, A., Shallue, C. J., et al. 2020, *Identifying Exoplanets with Deep Learning. IV. Removing Stellar Activity Signals from Radial Velocity Measurements Using Neural Networks*
- Delisle, J. B., Ségransan, D., Dumusque, X., et al. 2018, *A&A*, 614, A133
- Delisle, J. B., Unger, N., Hara, N. C., & Ségransan, D. 2022, *A&A*, 659, A182
- Deng, L. 2012, *IEEE Signal Processing Magazine*, 29, 141
- Devlin, J., Chang, M.-W., Lee, K., & Toutanova, K. 2019, in *Proceedings of the 2019 Conference of the North American Chapter of the Association for Computational Linguistics: Human Language Technologies, Volume 1 (Long and Short Papers)* (Minneapolis, Minnesota: Association for Computational Linguistics), 4171–4186
- Díaz, R. F., Delfosse, X., Hobson, M. J., et al. 2019, *A&A*, 625, A17
- Díaz, R. F., Ségransan, D., Udry, S., et al. 2016, *A&A*, 585, A134
- Díaz, R. F., Ségransan, D., Udry, S., et al. 2016, *A&A*, 585, A134
- Dreizler, S., Jeffers, S. V., Rodríguez, E., et al. 2020, *MNRAS*, 493, 536
- Dumusque, X., Santos, N. C., Udry, S., Lovis, C., & Bonfils, X. 2011a, *A&A*, 527, A82
- Dumusque, X., Udry, S., Lovis, C., Santos, N. C., & Monteiro, M. J. P. F. G. 2011b, *A&A*, 525, A140
- Espinoza, N., Kossakowski, D., & Brahm, R. 2019, *MNRAS*, 490, 2262
- Feng, F., Tuomi, M., Jones, H. R. A., et al. 2017, *AJ*, 154, 135
- Foreman-Mackey, D., Agol, E., Ambikasaran, S., & Angus, R. 2017a, *AJ*, 154, 220
- Foreman-Mackey, D., Agol, E., Ambikasaran, S., & Angus, R. 2017b, *AJ*, 154, 220
- Frodesen, A. G., Skjeggstad, O., & Tøfte, H. 1979, *Probability and statistics in Particle Physics* (Universitetsforlaget, 1979)
- Giles, H. A. C., Collier Cameron, A., & Haywood, R. D. 2017, *MNRAS*, 472, 1618
- Goodfellow, I., Bengio, Y., & Courville, A. 2016, *Deep Learning* (MIT Press), <http://www.deeplearningbook.org>
- Halevy, A., Norvig, P., & Pereira, F. 2009, *IEEE Intelligent Systems*, 24, 8
- Haywood, R. D., Collier Cameron, A., Queloz, D., et al. 2014, *MNRAS*, 443, 2517
- He, K., Zhang, X., Ren, S., & Sun, J. 2016, in *Proceedings of the IEEE conference on computer vision and pattern recognition*, 770–778
- Hertz, J., Krogh, A., & Palmer, R. G. 1991, *Introduction to the Theory of Neural Computation* (USA: Addison-Wesley Longman Publishing Co., Inc.)
- Howard, A. W., Marcy, G. W., Johnson, J. A., et al. 2010, *Science*, 330, 653

- Jurgenson, C., Fischer, D., McCracken, T., et al. 2016, in Society of Photo-Optical Instrumentation Engineers (SPIE) Conference Series, Vol. 9908, Ground-based and Airborne Instrumentation for Astronomy VI, ed. C. J. Evans, L. Simard, & H. Takami, 99086T
- Khan, M. S., Jenkins, J., & Yoma, N. 2017, IEEE Signal Processing Magazine, 34
- Krizhevsky, A., Sutskever, I., & Hinton, G. E. 2012, Advances in neural information processing systems, 25, 1097
- Landau, E. 2017, Overlooked Treasure: The First Evidence of Exoplanets, <https://www.jpl.nasa.gov/news/news.php?feature=6991>
- Lecun, Y., Bottou, L., Bengio, Y., & Haffner, P. 1998, Proceedings of the IEEE, 86, 2278
- Lefebvre, S., García, R. A., Jiménez-Reyes, S. J., Turck-Chièze, S., & Mathur, S. 2008, A&A, 490, 1143
- Lomb, N. R. 1976, Ap&SS, 39, 447
- Lovis, C., Dumusque, X., Santos, N. C., et al. 2011, A&A, submitted [arXiv:1107.5325]
- Lovis, C., Mayor, M., Pepe, F., et al. 2006, Nature, 441, 305
- Luque, R., Pallé, E., Kossakowski, D., et al. 2019, A&A, 628, A39
- Mamajek, E. E. & Hillenbrand, L. A. 2008, The Astrophysical Journal, 687, 1264
- Mayor, M., Pepe, F., Queloz, D., et al. 2003, The Messenger, 114, 20
- Mayor, M. & Queloz, D. 1995, Nature, 378, 355
- Mayor, M., Udry, S., Lovis, C., et al. 2009, A&A, 493, 639
- McCaulliff, S. D., Jenkins, J. M., Catanzarite, J., et al. 2015, The Astrophysical Journal, 806, 6
- Meunier, N., Desort, M., & Lagrange, A.-M. 2010, A&A, 512, A39
- Márquez-Neila, P., Fisher, C., Sznitman, R., & Heng, K. 2018, Nature Astronomy, 2
- Nelson, B. E., Ford, E. B., Buchner, J., et al. 2020, AJ, 159, 73
- Nielsen, M. B., Gizon, L., Schunker, H., & Karoff, C. 2013, A&A, 557, L10
- Osborn, H. P., Ansdell, M., Ioannou, Y., et al. 2020, A&A, 633, A53
- Pearson, K. A., Palafox, L., & Griffith, C. A. 2018, MNRAS, 474, 478
- Pepe, F., Cristiani, S., Rebolo, R., et al. 2021, A&A, 645, A96
- Perruchot, S., Kohler, D., Bouchy, F., et al. 2008, in SPIE Conference Series, Vol. 7014, SPIE Conference Series
- Persson, C. M., Fridlund, M., Barragán, O., et al. 2018, A&A, 618, A33
- Peters, M., Neumann, M., Iyyer, M., et al. 2018, in Proceedings of the 2018 Conference of the North American Chapter of the Association for Computational Linguistics: Human Language Technologies, Volume 1 (Long Papers) (New Orleans, Louisiana: Association for Computational Linguistics), 2227–2237
- Quirrenbach, A., Amado, P. J., Caballero, J. A., et al. 2014, in Society of Photo-Optical Instrumentation Engineers (SPIE) Conference Series, Vol. 9147, Ground-based and Airborne Instrumentation for Astronomy V, ed. S. K. Ramsay, I. S. McLean, & H. Takami, 91471F
- Rajpaul, V., Aigrain, S., Osborne, M. A., Reece, S., & Roberts, S. 2015, MNRAS, 452, 2269
- Rao, S., Mahabal, A., Rao, N., & Raghavendra, C. 2021, MNRAS, 502, 2845
- Rasmussen, C. E. & Williams, C. K. I. 2005, Gaussian Processes for Machine Learning (Adaptive Computation and Machine Learning) (The MIT Press)
- Saar, S. H. & Donahue, R. A. 1997, The Astrophysical Journal, 485, 319
- Saha, S., Mathur, A., Bora, K., Agrawal, S., & Basak, S. 2018
- Scargle, J. D. 1982, ApJ, 263, 835
- Schrijver, C. J. & Zwaan, C. 2000, Solar and Stellar Magnetic Activity, Cambridge Astrophysics (Cambridge University Press)
- Shallue, C. J. & Vanderburg, A. 2018, The Astronomical Journal, 155, 94
- Suárez Mascareño, A., Faria, J. P., Figueira, P., et al. 2020, A&A, 639, A77
- Udry, S., Dumusque, X., Lovis, C., et al. 2019, A&A, 622, A37
- VanderPlas, J. T. 2018, The Astrophysical Journal Supplement Series, 236, 16
- Waldmann, I. P. 2016, The Astrophysical Journal, 820, 107
- Wolszczan, A. & Frail, D. A. 1992, Nature, 355, 145 EP
- Wright, D. J., Wittenmyer, R. A., Tinney, C. G., Bentley, J. S., & Zhao, J. 2016, ApJ, 817, L20
- Yu, L., Donati, J. F., Hébrard, E. M., et al. 2017, MNRAS, 467, 1342
- Yu, L., Vanderburg, A., Huang, C., et al. 2019, AJ, 158, 25
- Zechmeister, M., Dreizler, S., Ribas, I., et al. 2019, A&A, 627, A49
- Zechmeister, M. & Kürster, M. 2009, A&A, 496, 577
- Zechmeister, M. & Kürster, M. 2009, A&A, 496, 577
- Zeiler, M. D. & Fergus, R. 2014, in Computer Vision—ECCV 2014: 13th European Conference, Zurich, Switzerland, September 6–12, 2014, Proceedings, Part I 13, Springer, 818–833
- Zucker, S. & Giryes, R. 2018, AJ, 155, 147

Appendix A: Convolutional Neural Networks

In this Appendix, we make a very brief summary of general concepts and usage of convolutional networks. Notions such as layer or backpropagation, and the generalities of artificial neurons (activation function, synaptic weight, bias, etc.) are assumed to be known. Those wishing to investigate further into theoretical and implementation concepts can refer to the bibliography (Bishop (2007); Hertz et al. (1991); Goodfellow et al. (2016)).

Deep fully-connected networks have achieved very good practical results used in a wide variety of problems. However, for the treatment of images, they have a disadvantage, they do not take into account the spatial structure of the image. As a consequence, they can become extremely inefficient. On the other hand, convolutional neural networks (CNN) were designed specifically to tackle tasks of computer vision. These networks use convolutions instead of classical matrix operations and were created to work with images, but are also useful for one-dimensional data where the structure of the data is relevant.

Broadly speaking, CNNs perform the following steps when processing an image:

- *Feature extraction*: Each neuron takes its synaptic inputs from a local receptive field, i.e. a small region in the previous layer, and combines them to extract local features.
- *Feature mapping*: Each layer of the network is made up of many feature maps, each in the form of a plane within which individual neurons are forced to share the same set of synaptic weights. This second form of structural restriction has the following beneficial effects:
 - Translational invariance, achieved by performing the convolution operation on a feature map with a small kernel, followed by applying the activation function. A kernel is a small matrix of weights with which the image is convoluted.
 - Reduced number of parameters, achieved through the use of shared weights.
- *Subsampling*: Convolutional layers are often followed by a layer that performs local averaging and subsampling, thus reducing the resolution of the feature map. This operation has the effect of reducing the sensitivity of the feature map output.

In this way, a deep network is obtained that in its first layers detects lines or curves; but, as it progresses, it detects more complex shapes such as a face or a silhouette (Zeiler & Fergus 2014).

To make a feature map, a kernel is applied to an image, this kernel on the image is the *receptive field* that a neuron “sees”. In Figure A.1, there is an example of how a characteristics map is generated. In the example, a 3x3 kernel is applied on a 5x5 image⁹.

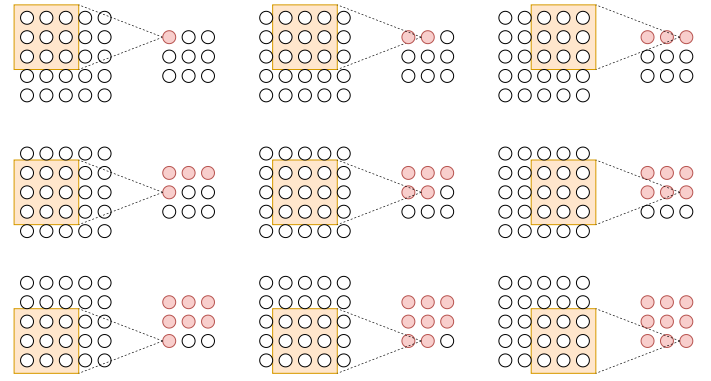


Fig. A.1: Generation of a feature map using one kernel.

The size of the kernel is one of the parameters chosen when creating the network. They are usually small to extract local characteristics. To find many of these features, many kernels are used. They all have the same dimension, but the weights they learn are different (they look for different things). This set of kernels is what is called a filter.

Next we focus on how downsampling layers work and why they are needed, using the classic MNIST dataset (Deng 2012) as an example. This dataset consists of tens of thousands of hand-written digit images, which are in black and white and with a resolution of 28x28 pixels. Each image represents a digit between zero and nine.

In Figure A.2 you can see how applying a filter of 32 kernels of 3x3 gives 32 activation maps of 26x26 each¹⁰, so the number of neurons in this first hidden layer is 21,632

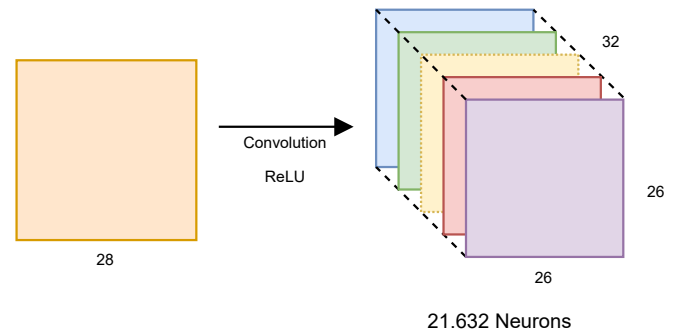


Fig. A.2: First hidden layer.

The size of the information after the first layer has increased considerably. Consider this is a very small image, and it is only the first layer. Adding more layers can make this number grow very fast. Eventually, this hinders training a network on large high-definition images, since the network will lose the ability to abstract. This is where the downsampling layer comes in.

The most used implementation is maxpooling. In this mechanism, we seek to reduce the parameters by dividing the input matrix into parts and keeping the maximum value of each one. It seeks to preserve the most important characteristics and reduce the dimensions of the data. In Figure A.3 there is an example of its application.

⁹ For simplicity, these examples are presented on matrices in two dimensions, assuming black and white images. If they were colour images it would be necessary to add a dimension to the input and the kernel. So we would have three filters, these three filters are added together with the *bias* and they will form an output as if it were a single channel.

¹⁰ The output dimension o to apply a kernel of dimensions k to an image of size w can be calculated with this formula: $o = w - k + 1$. Concepts such as padding or stride modify this formula, but they are unnecessary for the example.

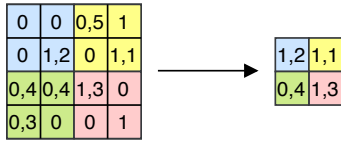
Fig. A.3: *Maxpooling*.

Figure A.4 shows the result of using this layer over the output of Figure A.2.

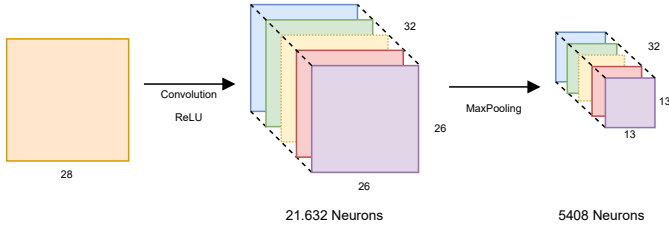


Fig. A.4: Use of maxpooling for dimensionality reduction.

As expected, the number of layers required to reach good performance, and the manner in which they are interleaved, depends on the problem to be solved, and there is no general rule. But in general, the convolutional network extracts the most relevant features from the image and then connects them to one or more fully connected layers and an output layer used for classification. This layer depends on the problem. In this particular example, it has a neuron for each category –i.e. ten neurons– and uses a softmax activation function. This activation function normalises the outputs of the output layer so that each value can be interpreted as the probability of belonging to a given class. The fully-connected part, together with the output layer use the information extracted in the convolutional part, and “decide” to which category the entry belongs. Figure A.5 shows a general diagram of the network in this example.

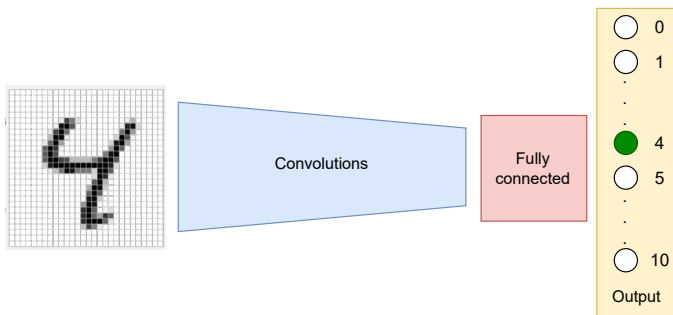


Fig. A.5: Full network.